Implementation of the density functional perturbation theory for generalized susceptibility in the projector augmented wave framework

Xiaoqiang Liu [1], Yihao Lin [1] and Ji Feng [1,2,*]

[1] *International Center for Quantum Materials, School of Physics, Peking University, Beijing 100871, China*

[2] *Hefei National Laboratory, Hefei 230088, China*

(Received 31 December 2022; revised 26 June 2023; accepted 11 August 2023; published 5 September 2023)

The quantification of materials' dynamical responses to external electromagnetic fields is central to understanding their physical properties. Here we present an implementation of the density functional perturbation theory for the computation of linear susceptibilities using the projector augmented wave method. The Sternheimer equations are solved self-consistently through a nested iterative procedure to compute the first-order wave functions, from which the linear susceptibilities are obtained. As a demonstration, we compute the spin-wave spectral functions of two magnetic metals. The computed magnon spectra for half-metallic CrO_2 and a Heusler intermetallic Cu_2MnAl show gapless Goldstone modes when spin-rotation symmetry is preserved and display reasonable agreement with available experimental data. The Landau damping is computed to be small in CrO_2, but significant in Cu_2MnAl, producing an asymmetric Lorentzian spectral line shape. The access to linear susceptibilities as well as first-order wave functions offers a range of novel possibilities in the quantitative understanding of materials' electronic properties from *ab initio* methods.

DOI: 10.1103/PhysRevB.108.094405

I. INTRODUCTION

A microscopic understanding of the electrical and magnetic characteristics of materials plays a key role in condensed matter physics, furnishing a unified insight into a wide range of phenomena. Indeed, the generalized density response functions (i.e., susceptibilities) of a many-electron system to external electromagnetic fields [1] in a broad sense encompass the information of the usual longitudinal dielectric function and magnetic permeability, as well as the cross terms for electromagnetic coupling. The properties of collective excitations, e.g., plasmon and magnon, can also be procured from the susceptibilities. Therefore, computing the susceptibilities, which involve both charge and spin degrees of freedom of electrons, is essential to a full characterization of electronic properties. Though relatively straightforward for a noninteracting system, computing the susceptibilities for an interacting many-electron system is a nontrivial task due to interaction effects.

The Kohn-Sham density functional theory (DFT) [2] is by far the most widely employed ground-state electronic structure method for materials and molecules. By mapping the interacting ground state to that of a noninteracting system with the same density and described by Kohn-Sham equations, the static density (and response) of a many-body system can be captured via a variational formulation of the Kohn-Sham systems. In the time-dependent (TD) DFT [3], the electrodynamics is described by TD Kohn-Sham equations. In these theories, the Hartree and exchange-correlation potentials are functionals of density and treated as self-consistent fields. The self-consistent first-order perturbation in TD DFT leads to the density functional perturbation theory (DFPT) [4], which is then the machinery for linear response calculations leading directly to the full response functions. Another approach to the response functions is the many-body perturbation theory [5–8] based on diagrammatic techniques.

DFPT-based methods have been successfully applied to calculate the dielectric function [9–13] and phonon dispersion [14–16], with the results in quantitative agreement with experimental observations. In the computations of dielectric function, the first-order wave functions with respect to $\boldsymbol{k}$ are solved, while the deformation potential from frozen atomic displacements is used as the external field to compute phonon dispersions. Dynamical responses to external electromagnetic fields from DFPT, which account for the screening of both charge and spin, have attracted considerable interest recently [17–24]. In addition to quantifying the electrical and magnetic properties of materials, the linear susceptibilities computed from DFPT also find applications in the *GW* approximations [25–27].

Approaches to the DFPT can be broadly grouped into two categories: a Dyson-like equation is solved in the first [18,19,24], whereas the Sternheimer equations are solved in the second [17,20–23]. The Dyson-like equation approach starts with response functions computed for the Kohn-Sham ground state, followed by solving a Dyson-like equation in the response function. Though formally transparent and amenable to various iterative techniques, this approach suffers from two shortcomings: it requires a large number of unoccupied states and huge plane-wave bases for adequate convergence [24], and more serious is the subtle basis set incompatibility between the Kohn-Sham states and the DFPT process, which gives rise to an artifactual spin excitation gap in systems with spin-rotation symmetry. The latter problem can only be partially mended with delicate engineering of the

*jfeng11@pku.edu.cn

interaction kernel [19,28]. In the second category, the first-order wave functions are procured (often iteratively) by solving the Sternheimer equations, from which the density is updated with charge mixing iterations and the response functions are computed upon convergence. In this case, one is forced to deal with wave functions and various pseudopotentials with all the technicalities [29–32], in addition to the nested iterative procedure. On the other hand, since the full Kohn-Sham response functions are never required, this method is free of the burden of summation over a huge number of empty states. In addition, the first-order wave functions and densities are computed as bonuses, which can be useful for computing a variety of properties.

A particularly popular plane-wave-based approach to DFT is based on the projector augmented wave (PAW) method [31,32]. Combining the formal simplicity of pseudopotentials and the versatility of the linearized augmented plane-wave method, the PAW method offers both efficiency and accuracy to Kohn-Sham DFT calculations on extended solids, and a wide range of capabilities in various implementations [33–35]. Despite its popularity, DFPT in the PAW framework has remained to be developed, which is accomplished in this work by solving the TD Sternheimer equations to compute the linear susceptibilities of crystalline materials accounting for both charge and spin degrees of freedom. The paper is organized as follows. In Sec. II A, the general theory of DFPT is introduced, and the dressed spin in TD external electromagnetic fields is defined. The screening built on the notion of dressed spin leads to the Sternheimer equations in the frequency and momentum domain and explicit formula for the linear susceptibilities. In Sec. II B, the PAW method is reviewed, based on which the formulation of DFPT in the PAW framework is described, along with a few implementation details. As a first calibration of our implementation, the spin-wave spectral functions are extracted from the computed linear susceptibilities. Two examples are presented: half-metallic CrO_2 (Sec. III A) shows a clean spin-wave spectrum and minimal Landau damping, and a full Heusler intermetallic Cu_2MnAl (Sec. III B) shows significant Landau damping in the spin excitations that can be quantified with a simple asymmetric Lorentzian line shape. Lastly, a summary is provided with an eye on room for development from both algorithm and physics points of view.

II. THEORY AND IMPLEMENTATION

A. Density functional perturbation theory

The TD DFT offers an efficient description of the dynamics of an interacting many-electron system in the presence of external fields [3]. As a self-consistent perturbation theory of TD DFT, DFPT is introduced in this section, wherein the Sternheimer equations are specialized to crystalline systems under a monochromatic, periodic external electromagnetic field.

In TD DFT, to account for both charge and spin degrees of freedom, the generalized density is given by

$$\begin{aligned}\rho(\boldsymbol{r},t) &= \sum_n \theta_n \psi_n^\dagger(\boldsymbol{r},t)\sigma\psi_n(\boldsymbol{r},t)\\ &= (\rho_0,\boldsymbol{m}) = (\rho_0,\rho_1,\rho_2,\rho_3),\end{aligned} \tag{1}$$

where θ_n is the occupancy of the spinor single-particle state $\psi_n^\dagger = (\psi_{n\uparrow}^\dagger, \psi_{n\downarrow}^\dagger)$, and the four-vector spin $\sigma = (\sigma_0,\sigma_1,\sigma_2,\sigma_3)$ (σ_0 is the identity matrix and σ_α with $\alpha = 1,2,3$ are the Pauli matrices). The atomic units [36] are adopted in this paper, so ρ_0 is the total charge density and $\boldsymbol{m}$ is the magnetization density. The dynamics of ψ_n is prescribed by the TD Kohn-Sham equations [3],

$$i\partial_t|\psi_n(t)\rangle = [H+\delta H(t)]|\psi_n(t)\rangle. \tag{2}$$

The ground-state Kohn-Sham Hamiltonian [2] in Eq. (2) is $H = -\frac{1}{2}\nabla^2 + v[\rho^{(0)}](\boldsymbol{r})$, where the self-consistent potential is a functional of the ground-state density $\rho^{(0)}$, composed of ionic, Hartree, and exchange-correlation (xc) potentials, namely, v^{i}, v^{H}, and v^{xc}. Though the xc potential v^{xc} as a functional of density is, in principle, nonlocal in space and time [37–41], the commonly adopted local and adiabatic approximation (ALDA) is assumed in this work [42–44].

The first-order Hamiltonian δH comprises two contributions. The first arises from the coupling of the four-vector spin σ with external fields,

$$v^{\mathrm{ext}}(\boldsymbol{r},t) = -B_\alpha(\boldsymbol{r},t)\sigma_\alpha, \tag{3}$$

where the four-vector electromagnetic field $B(\boldsymbol{r},t) = (-\phi,\frac{1}{2}\boldsymbol{B})$ [45]. Here, $\boldsymbol{B}$ is the Zeeman field. We ignore the nonlocal coupling between the magnetic field and orbitals, which requires the current density functional theory and is beyond the scope of the present work. The indices $\alpha,\beta = 0,1,2,3$ are implicitly summed over when repeated, but we will keep other summations explicit. The self-consistent inclusion of the density dependence in the Hartree and xc potentials means that δH also includes a second contribution from induced density $\delta\rho(\boldsymbol{r},t)$ that screens v^{ext}, which can be formulated as

$$\delta H^{\mathrm{ind}}(\boldsymbol{r},t) = \sigma_\alpha \int f_{\alpha\beta}(\boldsymbol{r},\boldsymbol{r}')\delta\rho_\beta(\boldsymbol{r}',t)d\boldsymbol{r}'. \tag{4}$$

The interaction kernel has two components, $f_{\alpha\beta} = f_{\alpha\beta}^{\mathrm{H}} + f_{\alpha\beta}^{\mathrm{xc}}$, namely, the Hartree and xc kernels in the ALDA,

$$f_{\alpha\beta}(\boldsymbol{r},\boldsymbol{r}') = \frac{\delta_{\alpha0}\delta_{\beta0}}{|\boldsymbol{r}-\boldsymbol{r}'|} + \frac{1}{2}\delta(\boldsymbol{r}-\boldsymbol{r}')\,\mathrm{tr}\left[\sigma_\alpha\frac{\partial v^{\mathrm{xc}}}{\partial\rho_\beta}\right]. \tag{5}$$

According to the linear response theory, we have

$$\delta\rho_\alpha(\boldsymbol{r},t) = \int \chi_{\alpha\beta}(\boldsymbol{r},\boldsymbol{r}',t-t')B_\beta(\boldsymbol{r}',t')d\boldsymbol{r}'dt', \tag{6}$$

where $\chi_{\alpha\beta}(\boldsymbol{r},\boldsymbol{r}',t)$ is the linear susceptibility that we pursue in this work. Thus, the first-order Hamiltonian can be written in terms of a *dressed spin* τ_α in unscreened external fields,

$$\delta H(\boldsymbol{r},t) = -\int \tau_\alpha(\boldsymbol{r},\boldsymbol{r}',t-t')B_\alpha(\boldsymbol{r}',t')d\boldsymbol{r}'dt', \tag{7}$$

which is defined via

$$\begin{aligned}\tau_\alpha(\boldsymbol{r},\boldsymbol{r}',t-t') &= -\frac{\delta H(\boldsymbol{r},t)}{\delta B_\alpha(\boldsymbol{r}',t')} = \sigma_\alpha\delta(\boldsymbol{r}-\boldsymbol{r}')\delta(t-t')\\ &\quad - \sigma_\gamma\int f_{\gamma\beta}(\boldsymbol{r},\boldsymbol{r}'')\chi_{\beta\alpha}(\boldsymbol{r}'',\boldsymbol{r}',t-t')d\boldsymbol{r}''.\end{aligned} \tag{8}$$

As elaborated below, the linear susceptibility can be expressed explicitly in terms of dressed spin.

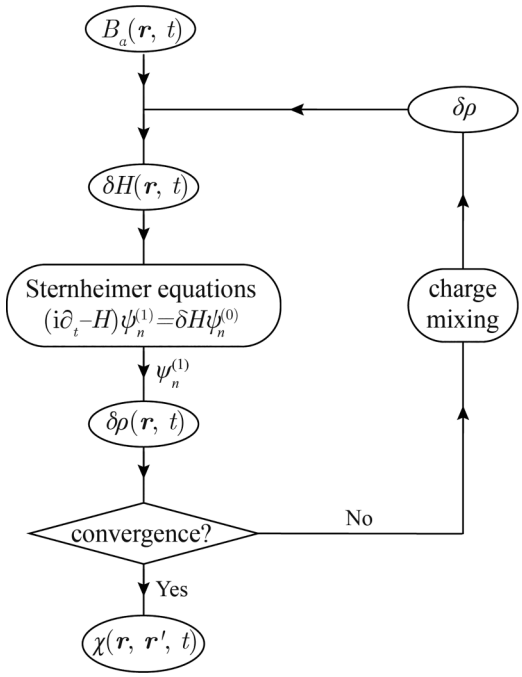

FIG. 1. Flow chart for a nested-loop DFPT calculation in the Sternheimer equation approach. The outer loop depicted here is the charge mixing. The inner loop is incurred in solving the Sternheimer equations in each step of the outer iteration.

Now with the first-order Hamiltonian, the first-order wave functions can be obtained by solving the Sternheimer equations [15,17,20,46–48],

$$(i\partial_t - H)\left|\psi_n^{(1)}(t)\right\rangle = \delta H(t)\left|\psi_n^{(0)}(t)\right\rangle, \tag{9}$$

in which $\psi_n^{(\ell)}(t)$ is the ℓth-order wave function, with $|\psi_n^{(0)}(t)\rangle = e^{-i\varepsilon_n t}|\psi_n\rangle$. With the first-order wave functions, we will be able to compute the induced density via the variation of Eq. (1), from which the first-order Hamiltonian will be updated.

With the above introduction, a DFPT calculation can then be performed in a nested iterative process depicted in Fig. 1. In the initializing step, δH is constructed from the external electromagnetic fields, whence the Sternheimer equations are solved in the inner iteration. This produces a set of first-order wave functions, from which the induced density is calculated. A charge mixing strategy [49,50] is employed to revise the induced density and a new δH is then constructed to enter a next outer iteration. The above process is repeated until convergence, with the linear susceptibility and dressed spin as the output.

We now explain how the Sternheimer equations are solved for a crystalline solid. For electrons in a crystal, the initial Kohn-Sham states are Bloch functions such that $|\psi_n\rangle \mapsto |\psi_{n\boldsymbol{k}}\rangle = e^{i\boldsymbol{k}\cdot\boldsymbol{r}}|u_{n\boldsymbol{k}}\rangle$, where n is the band index and $\boldsymbol{k}$ is the crystal momentum, and $u_{n\boldsymbol{k}}$ is the cell-periodic part of the Bloch function. The system is subject to spatially periodic and monochromatic external electromagnetic fields,

$$B_\alpha(\boldsymbol{r},t) = \mathscr{B}_\alpha e^{i(\boldsymbol{p}\cdot\boldsymbol{r}-\omega t)} + \text{c.c.}, \tag{10}$$

where $\boldsymbol{p} = \boldsymbol{q} + \boldsymbol{g}$, with $\boldsymbol{g}$ being a reciprocal lattice vector for $\boldsymbol{q}$ in the first Brillouin zone. In this case, the following expansion is useful:

$$\zeta(\boldsymbol{r},t) = \sum_\ell e^{i(\boldsymbol{l}\cdot\boldsymbol{r}-\nu t)}\zeta(\boldsymbol{r},\ell), \tag{11}$$

for $\zeta = \delta H, \delta\rho_\alpha$, in which $\zeta(\boldsymbol{r},\ell)$ is a time-independent cell-periodic function. Here, $\ell \equiv (\nu, \boldsymbol{l}, \boldsymbol{h})$, whose values can only be taken as $\pm(\omega, \boldsymbol{q}, \boldsymbol{g})$. Then the first-order Hamiltonian in the ℓ channel is

$$\begin{aligned}\delta H(\boldsymbol{r},\ell) = &- e^{i\boldsymbol{h}\cdot\boldsymbol{r}}\sigma_\alpha\mathscr{B}_\alpha(\ell) \\ &+ \sigma_\alpha\int f_{\alpha\beta}(\boldsymbol{r},\boldsymbol{r}')\delta\rho_\beta(\boldsymbol{r}',\ell)e^{i\boldsymbol{l}\cdot(\boldsymbol{r}'-\boldsymbol{r})}d\boldsymbol{r}',\end{aligned} \tag{12}$$

where $\mathscr{B}_\alpha(\omega,\boldsymbol{q},\boldsymbol{g}) = \mathscr{B}_\alpha$, $\mathscr{B}_\alpha(-\omega,-\boldsymbol{q},-\boldsymbol{g}) = (\mathscr{B}_\alpha)^*$.

The first-order wave function is expanded as

$$\left|\psi_{n\boldsymbol{k}}^{(1)}(t)\right\rangle = \sum_\nu e^{-i(\nu+\varepsilon_{n\boldsymbol{k}})t}\left|\psi_{n\boldsymbol{k}}^{(1)}(\nu)\right\rangle, \tag{13}$$

with

$$\left|\psi_{n\boldsymbol{k}}^{(1)}(\nu)\right\rangle = e^{i(\boldsymbol{k}+\boldsymbol{l})\cdot\boldsymbol{r}}\left|u_{n\boldsymbol{k}}^{(1)}(\ell)\right\rangle. \tag{14}$$

Then the Sternheimer equations become

$$(\nu + i\eta + \varepsilon_{n\boldsymbol{k}} - H_{\boldsymbol{k}+\boldsymbol{l}})\left|u_{n\boldsymbol{k}}^{(1)}(\ell)\right\rangle = \delta H(\boldsymbol{r},\ell)|u_{n\boldsymbol{k}}\rangle, \tag{15}$$

in which $H_{\boldsymbol{k}} = e^{-i\boldsymbol{k}\cdot\boldsymbol{r}}He^{i\boldsymbol{k}\cdot\boldsymbol{r}}$ is the Bloch Hamiltonian. A positive infinitesimal η is introduced on the left-hand side as a convergence factor to embody the causality structure of the linear susceptibility. In actual calculations, η takes finite values to ensure convergence with finite $\boldsymbol{k}$-mesh, especially for metals, and bestows finite broadening on spectral peaks.

From the first-order wave functions, we compute the first-order induced density as

$$\begin{aligned}\delta\rho_\alpha(\boldsymbol{r},\ell) = \sum_{n\boldsymbol{k}}\theta_{n\boldsymbol{k}}\big\{&u_{n\boldsymbol{k}}^\dagger(\boldsymbol{r})\sigma_\alpha u_{n\boldsymbol{k}}^{(1)}(\boldsymbol{r},\ell) \\ &+ u_{n\boldsymbol{k}}^{(1)^\dagger}(\boldsymbol{r},-\ell)\sigma_\alpha u_{n\boldsymbol{k}}(\boldsymbol{r})\big\}.\end{aligned} \tag{16}$$

The linear susceptibility can be extracted from the Fourier components of $\delta\rho_\alpha(\boldsymbol{r},\ell)$,

$$\delta\rho_\alpha(\boldsymbol{g}',\ell) = \chi_{\alpha\beta}(\boldsymbol{g}',\ell)\mathscr{B}_\beta(\ell),$$

whence

$$\chi_{\alpha\beta}(\boldsymbol{g}',\ell) = \int e^{-i(\boldsymbol{g}'+\boldsymbol{l})\cdot\boldsymbol{r}}\chi_{\alpha\beta}(\boldsymbol{r},\boldsymbol{r}',\nu)e^{i(\boldsymbol{h}+\boldsymbol{l})\cdot\boldsymbol{r}'}d\boldsymbol{r}d\boldsymbol{r}'. \tag{17}$$

It is worth mentioning that if we write the first-order Hamiltonian in Eq. (12) in terms of the dressed spin,

$$\begin{aligned}\delta H(\boldsymbol{r},\ell) &= - e^{-i\boldsymbol{l}\cdot\boldsymbol{r}}\tau_\alpha(\boldsymbol{r},\ell)\mathscr{B}_\alpha(\ell), \\ \tau_\alpha(\boldsymbol{r},\ell) &= \int\tau_\alpha(\boldsymbol{r},\boldsymbol{r}',t)e^{i[(\boldsymbol{l}+\boldsymbol{h})\cdot\boldsymbol{r}'+\nu t]}d\boldsymbol{r}'dt,\end{aligned} \tag{18}$$

then the Sternheimer equations in Eq. (15) admit the following formal solutions in the ℓ channel:

$$\left|u_{n\boldsymbol{k}}^{(1)}(\ell)\right\rangle = -\mathscr{B}_\alpha(\ell)\sum_{n'}\frac{|u_{n'\boldsymbol{k}+\boldsymbol{l}}\rangle\tau_\alpha(\boldsymbol{k},\ell)_{n'n}}{\nu+\varepsilon_{n\boldsymbol{k}}-\varepsilon_{n'\boldsymbol{k}+\boldsymbol{l}}+i\eta}, \tag{19}$$

in which the dressed spin matrix element is

$$\tau_\alpha(\boldsymbol{k},\ell)_{n'n} = \int u^\dagger_{n'\boldsymbol{k}+\boldsymbol{l}}(\boldsymbol{r})e^{-i\boldsymbol{l}\cdot\boldsymbol{r}}\tau_\alpha(\boldsymbol{r},\ell)u_{n\boldsymbol{k}}(\boldsymbol{r})d\boldsymbol{r}. \tag{20}$$

Because it requires the summation over a large number of empty states, this formal solution is not used in practice [51]. As will be explained later, in our implementation the exact solution is used to quickly correct the contributions of occupied and a small number of low-lying particle states in the iterative solution of the Sternheimer equations. The screened susceptibility then has the same expression as the (bare) Kohn-Sham susceptibility, except that the (unscreened) external fields are now coupled to the dressed spin; that is,

$$\chi_{\alpha\beta}(\boldsymbol{g}',\ell) = -\sum_{nn'\boldsymbol{k}}(\theta_{n\boldsymbol{k}}-\theta_{n'\boldsymbol{k}+\boldsymbol{l}}) \times \frac{\langle u_{n\boldsymbol{k}}|e^{-i\boldsymbol{g}'\cdot\boldsymbol{r}}\sigma_\alpha|u_{n'\boldsymbol{k}+\boldsymbol{l}}\rangle\tau_\beta(\boldsymbol{k},\ell)_{n'n}}{\nu+\varepsilon_{n\boldsymbol{k}}-\varepsilon_{n'\boldsymbol{k}+\boldsymbol{l}}+i\eta}. \tag{21}$$

In arriving at the last expression, we have used the fact that $\tau_\alpha(\boldsymbol{k},\ell)_{n'n} = \tau_\alpha(\boldsymbol{k}+\boldsymbol{l},-\ell)^*_{nn'}$. Recalling that the dressed spin in Eq. (8) is defined via the screened susceptibility, this in fact leads to the Dyson-like equation in χ.

B. DFPT with PAW method

The previous section presents a sketch of the DFPT for periodic systems without recourse to computational details. In practical calculations, however, various technologies have been developed such that one can perform DFT (and, therefore, DFPT) calculations on valence electrons only for crystalline materials using plane-wave bases with the aid of pseudopotentials to yield satisfactory accuracy with high efficiencies. It is well known that the norm-conserving pseudopotential [29] requires large plane-wave bases (particularly for localized orbitals in transition elements), while the application of an ultrasoft pseudopotential [30] is partly limited by the rather laborious construction. In contrast, the PAW method, combining the pseudopotential and linearized augmented plane-wave methods, is free from the above difficulties and has been widely used. Thus, performing DFPT within the PAW framework [31,32] for inhomogeneous and TD electromagnetic fields is evidently useful, though notably nontrivial.

DFPT with the PAW method has been implemented within the Vienna *ab initio* simulation package (VASP) [33] for atomic displacements in the static and long-wavelength limit to calculate zone-center phonon energies. The extension to inhomogeneous and TD electromagnetic fields is accomplished in this work based on VASP 5.4.4, and a few implementation details warrant further clarification. Here, we will briefly review the PAW method and describe how it is used in our DFPT calculations. Although the formalism for the ground-state quantities is identical to those in the literature and notationally notorious, we feel compelled to provide some of these details, particularly in view of the time- and position-dependent external fields involved in our implementation. The key of this endeavor is to express various parts of the densities in the PAW framework in monochromatic external potentials that allows efficient and accurate determination of the various parts of the induced potentials.

The PAW method is based on a linear transformation between the all-electron (AE) Hilbert space orthogonal to core states and pseudo (PS) Hilbert space. The AE and PS wave functions are related by

$$|\psi_{n\boldsymbol{k}}\rangle = T|\tilde{\psi}_{n\boldsymbol{k}}\rangle, \tag{22}$$

with the linear operator defined as

$$T = 1 + \sum_{ia}\left(|\phi^a_i\rangle - |\tilde{\phi}^a_i\rangle\right)\langle\tilde{p}^a_i|. \tag{23}$$

The index $i = (nlms)$ is a shorthand encapsulating the quantum numbers (nlm) of the local orbitals and spin s for the atomic site located at $\boldsymbol{R}_a$. ϕ, $\tilde{\phi}$, and $\tilde{p}$ are AE partial waves, PS partial waves, and projector functions, respectively, and should all be understood as spinors. In order to perform the DFPT calculations on a crystalline solid in the electromagnetic fields in Eq. (10), the key is to find the cell-periodic part of each PAW-pseudized quantity, especially the nonlocal ones.

Upon application of the time-independent transformation T to the first-order wave functions, the pseudized Sternheimer equations read

$$(i\partial_t S - \tilde{H})\left|\tilde{\psi}^{(1)}_{n\boldsymbol{k}}(t)\right\rangle = \delta\tilde{H}(t)\left|\tilde{\psi}^{(0)}_{n\boldsymbol{k}}(t)\right\rangle, \tag{24}$$

with $S = T^\dagger T$, $\tilde{H} = T^\dagger H T$, and $\delta\tilde{H}(t) = T^\dagger\delta H(t)T$.

According to the implementation of the PAW method in VASP (see Appendix A for a brief introduction) [32], we have

$$\begin{aligned} S &= 1 + \sum_{ija}|\tilde{p}^a_i\rangle q^a_{ij}\langle\tilde{p}^a_j|, \\ \tilde{H} &= -\frac{1}{2}\Delta + \tilde{v}^{\text{eff}} + \sum_{ija}|\tilde{p}^a_i\rangle\left(\hat{D}^a_{ij}+\tilde{D}^a_{ij}\right)\langle\tilde{p}^a_j|. \end{aligned} \tag{25}$$

Here the local potential $\tilde{v}^{\text{eff}}(\boldsymbol{r})$ is a functional of the sum of pseudodensity $\tilde{n}(\boldsymbol{r})$ and compensation density $\hat{n}(\boldsymbol{r})$, while the nonlocal potential $\tilde{D}^a_{ij}$ is a function of density matrix ϱ^a, i.e.,

$$\begin{aligned} \tilde{v}^{\text{eff}} &= \tilde{v}^{\text{eff}}[\tilde{n}+\hat{n}], \\ \hat{D}^a_{ij} &= \int_{\Omega_a}\tilde{v}^{\text{eff}}_\alpha(\boldsymbol{r})\hat{Q}^{a\alpha}_{ij}(\boldsymbol{r})d\boldsymbol{r}, \\ \tilde{D}^a_{ij} &= \tilde{D}^a_{ij}(\varrho^a). \end{aligned} \tag{26}$$

The definitions of q^a_{ij} and $\hat{Q}^{a\alpha}_{ij}(\boldsymbol{r})$ can be found in Appendix A. We have hidden the functional dependence on the pseudized core densities in $\tilde{v}^{\text{eff}}(\boldsymbol{r})$, which are kept frozen during the DFPT calculations. $\tilde{n}(\boldsymbol{r})$, $\hat{n}(\boldsymbol{r})$, and ϱ^a_{ij} are given by, respectively,

$$\begin{aligned} \tilde{n}_\alpha(\boldsymbol{r}) &= \sum_{n\boldsymbol{k}}\theta_{n\boldsymbol{k}}\tilde{\psi}^\dagger_{n\boldsymbol{k}}(\boldsymbol{r})\sigma_\alpha\tilde{\psi}_{n\boldsymbol{k}}(\boldsymbol{r}), \\ \hat{n}_\alpha(\boldsymbol{r}) &= \sum_{ija}\varrho^a_{ij}\hat{Q}^{a\alpha}_{ij}(\boldsymbol{r}), \\ \varrho^a_{ij} &= \sum_{n\boldsymbol{k}}\theta_{n\boldsymbol{k}}\langle\tilde{\psi}_{n\boldsymbol{k}}|\tilde{p}^a_i\rangle\langle\tilde{p}^a_j|\tilde{\psi}_{n\boldsymbol{k}}\rangle. \end{aligned} \tag{27}$$

Now we derive the expression for the first-order Hamiltonian $\delta\tilde{H}(t)$. For the fields in Eq. (10), the first-order local

densities and potentials follow the same expansion as in Eq. (11), while the first-order density matrix $\delta\varrho^a_{ij}$ and nonlocal potential δD^a_{ij} can be expanded as

$$\delta\zeta^a_{ij}(t) = \sum_\ell e^{i(\boldsymbol{l}\cdot\boldsymbol{R}_a - \nu t)}\delta\zeta^a_{ij}(\ell). \tag{28}$$

Here, the factor $e^{i\boldsymbol{l}\cdot\boldsymbol{R}_a}$ in the ℓ channel is introduced such that $\delta\zeta^a_{ij}(\ell)$ is cell periodic.

The contribution of external electromagnetic fields in $\delta\tilde{H}(t)$ can be calculated directly,

$$\begin{aligned}\delta\tilde{H}^{\rm ext}(\boldsymbol{r},t) = \sum_\ell e^{-i\nu t}\Bigg[& e^{i\boldsymbol{l}\cdot\boldsymbol{r}}v^{\rm ext}(\boldsymbol{r},\ell) \\ & + \sum_{ija} e^{i\boldsymbol{l}\cdot\boldsymbol{R}_a}\big|\tilde{p}^a_i\big\rangle D^{a,{\rm ext}}_{ij}(\ell)\big\langle\tilde{p}^a_j\big|\Bigg],\end{aligned} \tag{29}$$

with

$$\begin{aligned} v^{\rm ext}(\boldsymbol{r},\ell) =& -\mathscr{B}_\alpha(\ell)\sigma_\alpha e^{i\boldsymbol{h}\cdot\boldsymbol{r}}, \\ D^{a,{\rm ext}}_{ij}(\ell) =& \big\langle\phi^a_i\big|e^{i\boldsymbol{l}\cdot(\boldsymbol{r}-\boldsymbol{R}_a)}v^{\rm ext}(\boldsymbol{r},\ell)\big|\phi^a_j\big\rangle \\ & - \big\langle\tilde{\phi}^a_i\big|e^{i\boldsymbol{l}\cdot(\boldsymbol{r}-\boldsymbol{R}_a)}v^{\rm ext}(\boldsymbol{r},\ell)\big|\tilde{\phi}^a_j\big\rangle. \end{aligned} \tag{30}$$

The contribution to $\delta\tilde{H}(t)$ from the induced densities has an expression similar to Eq. (29) and can be calculated via an explicit finite difference, as $\tilde{H}$ is a functional of $\tilde{n}$, $\hat{n}$, and ϱ^a. The first-order densities are found to be

$$\begin{aligned} \delta\tilde{n}_\alpha(\boldsymbol{r},\ell) =& \sum_{n\boldsymbol{k}}\theta_{n\boldsymbol{k}}\big\{\tilde{u}^\dagger_{n\boldsymbol{k}}(\boldsymbol{r})\sigma_\alpha\tilde{u}^{(1)}_{n\boldsymbol{k}}(\boldsymbol{r},\ell) + \tilde{u}^{(1),\dagger}_{n\boldsymbol{k}}(\boldsymbol{r},-\ell)\sigma_\alpha\tilde{u}_{n\boldsymbol{k}}(\boldsymbol{r})\big\}, \\ \delta\hat{n}_\alpha(\boldsymbol{r},\ell) =& \sum_{ija} e^{i\boldsymbol{l}(\boldsymbol{R}_a-\boldsymbol{r})}\delta\varrho^a_{ij}(\ell)\hat{Q}^{a\alpha}_{ij}(\boldsymbol{r}), \\ \delta\varrho^a_{ij}(\ell) =& \sum_{n\boldsymbol{k}}\theta_{n\boldsymbol{k}}\big[\big\langle\tilde{u}_{n\boldsymbol{k}}\big|\tilde{p}^a_{i\boldsymbol{k}}\big\rangle\big\langle\tilde{p}^a_{j\boldsymbol{k}+\boldsymbol{l}}\big|\tilde{u}^{(1)}_{n\boldsymbol{k}}(\ell)\big\rangle \\ & + \big\langle\tilde{u}^{(1)}_{n\boldsymbol{k}}(-\ell)\big|\tilde{p}^a_{i\boldsymbol{k}-\boldsymbol{l}}\big\rangle\big\langle\tilde{p}^a_{j\boldsymbol{k}}|\tilde{u}_{n\boldsymbol{k}}\big\rangle\big], \end{aligned} \tag{31}$$

where we define $|\tilde{p}^a_{i\boldsymbol{k}}\rangle = e^{-i\boldsymbol{k}\cdot(\boldsymbol{r}-\boldsymbol{R}_a)}|\tilde{p}^a_i\rangle$. The first-order effective local potential is then given by

$$\begin{aligned}\delta\tilde{v}^{\rm eff}(\boldsymbol{r},\ell) = \int \left.\frac{\delta\tilde{v}^{\rm eff}(\boldsymbol{r})}{\delta n(\boldsymbol{r}')}\right|_{n=\tilde{n}+\hat{n}} & [\delta\tilde{n}(\boldsymbol{r}',\ell) \\ & + \delta\hat{n}(\boldsymbol{r}',\ell)]e^{i\boldsymbol{l}\cdot(\boldsymbol{r}'-\boldsymbol{r})}d\boldsymbol{r}'.\end{aligned} \tag{32}$$

The first-order Hartree term can be calculated directly in reciprocal space, while the first-order xc potential in the ALDA is approximated as

$$\delta\tilde{v}^{\rm xc}(\boldsymbol{r},\ell) \approx \tilde{v}^{\rm xc}[\tilde{n}+\hat{n}+\delta\tilde{n}(\ell)+\delta\hat{n}(\ell)] - \tilde{v}^{\rm xc}[\tilde{n}+\hat{n}]. \tag{33}$$

Similarly, the first-order nonlocal potentials can be approximated as

$$\begin{aligned}\delta\hat{D}^a_{ij}(\ell) =& \int_{\Omega_a} e^{i\boldsymbol{l}\cdot(\boldsymbol{r}-\boldsymbol{R}_a)}\delta\tilde{v}^{\rm eff}_\alpha(\boldsymbol{r},\ell)Q^{a\alpha}_{ij}(\boldsymbol{r})d\boldsymbol{r}, \\ \delta\tilde{D}^a_{ij}(\ell) =& \sum_{kl}\frac{\partial\tilde{D}^a_{ij}}{\partial\varrho^a_{kl}}\delta\varrho^a_{kl}(\ell) \\ \approx& \tilde{D}^a_{ij}[\varrho^a+\delta\varrho^a(\ell)] - \tilde{D}^a_{ij}(\varrho^a).\end{aligned} \tag{34}$$

Though introduced as forward differences in Eqs. (33) and (34), these quantities are evaluated using fourth-order centered finite differences, with a step length of a thousandth of the density variables.

With the above results, the final Sternheimer equations become

$$(\nu S_{\boldsymbol{k}+\boldsymbol{l}} + \varepsilon_{n\boldsymbol{k}}S_{\boldsymbol{k}+\boldsymbol{l}} - \tilde{H}_{\boldsymbol{k}+\boldsymbol{l}})\big|\tilde{u}^{(1)}_{n\boldsymbol{k}}(\ell)\big\rangle = \delta\tilde{H}_{\boldsymbol{k}}(\ell)|\tilde{u}_{n\boldsymbol{k}}\rangle, \tag{35}$$

with

$$\begin{aligned} S_{\boldsymbol{k}+\boldsymbol{l}} =& 1 + \sum_{ija}\big|\tilde{p}^a_{i\boldsymbol{k}+\boldsymbol{l}}\big\rangle q^a_{ij}\big\langle\tilde{p}^a_{j\boldsymbol{k}+\boldsymbol{l}}\big|, \\ \tilde{H}_{\boldsymbol{k}+\boldsymbol{l}} =& -\frac{1}{2}\Delta_{\boldsymbol{k}+\boldsymbol{l}} + \tilde{v}^{\rm eff} + \sum_{ija}\big|\tilde{p}^a_{i\boldsymbol{k}+\boldsymbol{l}}\big\rangle\big(\hat{D}^a_{ij}+\tilde{D}^a_{ij}\big)\big\langle\tilde{p}^a_{j\boldsymbol{k}+\boldsymbol{l}}\big|, \\ \delta\tilde{H}_{\boldsymbol{k}}(\ell) =& v^{\rm ext}(\ell) + \delta\tilde{v}^{\rm eff}(\ell) + \sum_{ija}\big|\tilde{p}^a_{i\boldsymbol{k}+\boldsymbol{l}}\big\rangle\big[D^{a,{\rm ext}}_{ij}(\ell) + \delta\hat{D}^a_{ij}(\ell) \\ & + \delta\tilde{D}^a_{ij}(\ell)\big]\big\langle\tilde{p}^a_{j\boldsymbol{k}}\big|. \end{aligned} \tag{36}$$

Here, $\tilde{u}_{n\boldsymbol{k}}$ and $\tilde{u}^{(1)}_{n\boldsymbol{k}}(\ell)$ are the cell-periodic parts of corresponding pseudo-wave functions, respectively.

Moreover, additional terms should be involved in the nonlocal potential when considering the spin-orbit coupling and the local-spin-density approximation plus the multiorbital mean-field Hubbard model (LSDA + U method), both of which are functions of the density matrix, i.e., $D^{a,{\rm SOC}}_{ij}(\varrho^a)$ and $D^{a,U}_{ij}(\varrho^a)$ (see Appendix A). The corresponding first-order contributions $\delta D^{a,{\rm SOC}}_{ij}(\ell)$ and $\delta D^{a,U}_{ij}(\ell)$ can be computed in a way similar to Eq. (34).

The pseudized Sternheimer equations in the $\pm(\omega,\boldsymbol{q},\boldsymbol{g})$ channels are solved separately in each iteration using a variant of the residual minimization method with a direct inversion in the iterative subspace (RMM-DIIS) [52,53], which is already implemented in VASP 5.4.4. The Löwdin perturbation theory is also performed to correct the first-order wave functions in the subspace of occupied states and low-lying excitations to speed up convergence,

$$\begin{aligned}\big|\tilde{u}^{(1)}_{n\boldsymbol{k}}(\ell)\big\rangle \to \big|\tilde{u}^{(1)}_{n\boldsymbol{k}}(\ell)\big\rangle - \sum_{n'}|\tilde{u}_{n'\boldsymbol{k}+\boldsymbol{l}}\rangle\big\langle\tilde{u}_{n'\boldsymbol{k}+\boldsymbol{l}}|S_{\boldsymbol{k}+\boldsymbol{l}}\big|\tilde{u}^{(1)}_{n\boldsymbol{k}}(\ell)\big\rangle \\ + \sum_{n'}\frac{|\tilde{u}_{n'\boldsymbol{k}+\boldsymbol{l}}\rangle\langle\tilde{u}_{n'\boldsymbol{k}+\boldsymbol{l}}|\delta\tilde{H}|\tilde{u}_{n\boldsymbol{k}}\rangle}{\nu+\varepsilon_{n\boldsymbol{k}}-\varepsilon_{n'\boldsymbol{k}+\boldsymbol{l}}}.\end{aligned} \tag{37}$$

In the last equation above, the summations on n' run over the occupied bands plus a few empty bands. In our practice, if the Löwdin perturbation theory is not performed, the results fail to converge within 80 charge mixing steps. This is because the projections of occupied states dominate the first-order wave functions due to the small energy differences and, without Löwdin perturbation correction, it will spend more time to search in the occupied subspace, which, however, has no contribution to the charge density.

Apparently, solving Eq. (35) requires a $\boldsymbol{k}$-grid supplemented by two additional grids shifted by $\pm\boldsymbol{q}$ when $\boldsymbol{q}$ itself is not on the $\boldsymbol{k}$-grid. Doing so, however, not only increases the computational burden but also, more seriously, obliterates the exact cancellation of the contribution of the occupied manifold to the density change due to a $\boldsymbol{k}$-grid discretization error. The latter can be easily avoided by employing a pair of

TABLE I. Reported implementations of DFPT for spin-wave spectra calculations by solving the Sternheimer equations.

Lead author (year)	Potential	Basis set	Software
Savrasov (1998) [17]	Full potential	LMTO[1]	LMTO MAGNONS
Cao *et al.* (2018) [20]	NCPP[2], USPP[3]	Plane wave	QE[4]
Gorni *et al.* (2018) [21]	NCPP	Plane wave	QE
Tancogne-Dejean *et al.* (2020) [22]	NCPP	Real space	OCTOPUS
Singh *et al.* (2020) [23]	Full potential	LAPW[5]	ELK

[1]Linear muffin-tin orbital; [2]Norm-conserving pseudopotential; [3]Ultrasoft pseudopotential; [4]QUANTUM ESPRESSO; [5]Linearized augmented plane wave.

grids with a $\boldsymbol{q}$ shift, which also partly reduces the calculation. Then Eq. (35) is solved on the $\boldsymbol{k}$-grid in the $+\boldsymbol{q}$ channel, and on the $\boldsymbol{k}+\boldsymbol{q}$ grid in the $-\boldsymbol{q}$ channel. It is observed that in this dual grid setup, the above cancellation is well preserved.

The xc potentials in ALDA are functionals of real-valued densities. Thus, calculating $\delta\tilde{v}^{\mathrm{xc}}(\ell)$, such as in Eq. (33), requires caution as $\delta\tilde{n}(\ell)$ and $\delta\hat{n}(\ell)$ are usually complex. In fact, the real and imaginary parts of $\delta\tilde{v}^{\mathrm{xc}}(\ell)$ are calculated separately,

$$\mathfrak{F}\delta\tilde{v}^{\mathrm{xc}}(\ell) \approx \tilde{v}^{\mathrm{eff}}[\tilde{n}+\hat{n}+\mathfrak{F}\delta\tilde{n}(\ell)+\mathfrak{F}\delta\hat{n}(\ell)] - \tilde{v}^{\mathrm{eff}}[\tilde{n}+\hat{n}], \tag{38}$$

where $\mathfrak{F}=\mathrm{Re},\mathrm{Im}$ takes the real or imaginary part, respectively. In the case of the nonlocal potential, $\delta\tilde{D}^{a}_{ij}(\ell)$ and $\delta\varrho^{a}_{ij}(\ell)$ are first decomposed into two independent Hermitian matrices (i.e., the Hermitian part and $-i$ times the anti-Hermitian part), and then finite differenced separately in an analogous fashion.

Symmetry reduction is also performed in our implementation, where the summation over $\boldsymbol{k}$ points in Eq. (31) is restricted to the symmetry-irreducible part of the Brillouin zone. The symmetry group here is the subgroup of the magnetic group of the studied crystal in which the external electromagnetic fields in Eq. (10) are invariant.

III. APPLICATION TO SPIN-WAVE SPECTRUM CALCULATION

Our implementation enables computing the linear susceptibilities $\chi_{\alpha\beta}$ with the self-consistent inclusion of the interaction kernel. Directly inverting $\chi_{\alpha\beta}$ yields the dielectric tensor, which is composed of the usual charge sector ϵ_{00}, spin sector $\epsilon_{\alpha\beta}$, and the spin-charge sector $\epsilon_{0\beta}$, each embodying unique physics. Computing $\chi_{\alpha\beta}$ then can have diverse applications in evaluating materials properties pertaining to both charge and spin fluctuations, or in subsequent many-body calculations beyond the Kohn-Sham mean fields. One immediate application that has received considerable attention is the calculation of spin-wave excitation [17–24]. According to the fluctuation-dissipation theorem, the spin-spin correlation function, directly accessible by various spin-sensitive inelastic scattering probes [54–56], is related to the imaginary part of the linear susceptibilities,

$$S_{+-}(\boldsymbol{p},\omega) = \frac{\mathrm{Im}\,\chi_{+-}(\boldsymbol{p},\omega)}{1-e^{-\hbar\omega/k_{\mathrm{B}}T}}. \tag{39}$$

For notational convenience, we have defined $\chi_{+-}(\boldsymbol{p},\omega) \equiv \chi_{+-}(\boldsymbol{g},\omega,\boldsymbol{q},\boldsymbol{g})$ as $\boldsymbol{p}=\boldsymbol{q}+\boldsymbol{g}$.

Although, for magnetic systems dominated by local moments, the magnon can be described effectively by localized spin models, this method is subject to debate when delocalization sets in, and ultimately of questionable validity for itinerant magnetism. In these latter cases, which include a wide range of magnetic materials, the DFPT route becomes invaluable for computing the spin-wave spectra *ab initio*. To our knowledge, there have been just a handful of works devoted to implementing the DFPT scheme for this purpose by solving the Sternheimer equations, as summarized in Table I. In these efforts, implementations are limited to the full potential [17,23], or norm-conserving and ultrasoft pseudopotentials [20–22].

In this section, we present an initial application of our implementation of DFPT in the PAW framework to the calculations of spin-wave spectra for a couple of magnetic materials. For ferromagnets with the spin polarized along the z direction, the transverse magnetic field can be applied by choosing $\mathscr{B}=(0,1,-i,0)$ in Eq. (10), from which χ_{+-} is directly calculated. In these cases, the only remaining symmetry operation keeping the crystal and the transverse magnetic field unchanged is identity transformation. Thus, there is no room for symmetry reduction.

A. Half-metallic chromium dioxide

As shown in the inset in Fig. 2, chromium dioxide CrO_2 is a ferromagnetic half-metallic oxide with a rutile crystal structure, where each Cr atom is situated at the center of an octahedral cage formed by oxygen atoms [57,58]. Widely used as a magnetic recording material, CrO_2 also has various potential applications in spintronics and magnetoelectronics [59,60] due to its half-metallic properties.

The experimental lattice parameters $a=b=4.4218$ Å and $c=2.9182$ Å [58] are used in our calculations. The plane-wave energy cutoff is set to be 500 eV and a $13\times13\times20$ Γ-centered mesh of $\boldsymbol{k}$ points is used. For the Brillouin zone integration, the tetrahedron method with Blöchl corrections is used in all subsequent calculations [61]. The spin-resolved densities of states of CrO_2 are computed from the collinear spin-polarized calculation and shown in Fig. 2, where the half-metallic nature is clearly seen. The magnetic moment of Cr is found to be $\sim2\ \mu_{\mathrm{B}}$. We then turn to the noncollinear calculations and compute the transverse spin susceptibility $\chi_{+-}(\boldsymbol{p},\omega)$ along the [100] and [001] directions for $\omega\leqslant400$ meV in 10 meV intervals. The broadening parameter η introduced in Eq. (15) is set to be 50 meV in the calculations in this section. Increasing the numbers of $\boldsymbol{k}$ points or reducing the value of

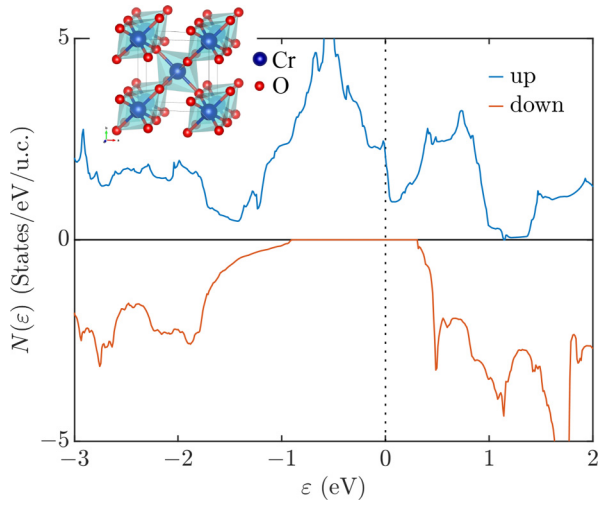

FIG. 2. Spin-resolved densities of states of CrO_2. The spin-flip gap is found to be about 310 meV. Inset: The crystal structure of CrO_2, highlighting the CrO_6 octahedra.

η has negligible effects on the energies of the magnons (see Appendix B).

Figure 3(a) shows the computed $\mathrm{Im}\chi_{+-}(\boldsymbol{p},\omega)$, without spin-orbit interaction, along two $\boldsymbol{p}$ paths. In general, $\chi_{+-}(\boldsymbol{p},\omega)$ is not periodic in $\boldsymbol{p}$. Then the branch in the first Brillouin zone is composed of acoustic magnon modes, while the branch in the second Brillouin zone is composed of optical modes. The profile of the magnon peak at a given $\boldsymbol{p}$ is a nearly perfect Lorentzian over the entire energy range. The extracted half width at half maximum $\eta_{\boldsymbol{p}}$ are almost a constant and equal to the artificial broadening parameter η, indicating that the Landau damping in CrO_2 is negligible. This is expected given that half-metallic CrO_2 has a large spin-flip gap around 310 meV, as shown in Fig. 2. The computed bare susceptibilities $\mathrm{Im}\chi^0_{+-}(\boldsymbol{p},\omega)$ shown in Fig. 3(b) for $\omega \leqslant 600$ meV also support such conclusion, where the Stoner continuum is found at energy above 450 meV near the Brillouin zone center.

The locations of the maxima of magnon peaks, ω_p, are then recorded and folded to the first Brillouin zone ($\omega_{\boldsymbol{q}}$). As shown in Fig. 3(c), we find one acoustic magnon branch and one optical branch, consistent with the fact that the unit cell in CrO_2 contains two magnetic Cr atoms. There is no magnon gap at the Brillouin zone boundaries, which is a result of the n glide symmetry. The energy of long-wavelength acoustic magnons is quadratic in q with a gapless Goldstone mode, $\omega_{\boldsymbol{q}} = D_{\parallel}(q_x^2 + q_y^2) + D_z q_z^2$, as expected for a ferromagnet with spin-rotation symmetry. The spin stiffness coefficients are found to be $D_{\parallel} = 82$ meV Å^2 along the [100] and $D_z = 92$ meV Å^2 along the [001] directions, respectively. From this, we can estimate the average spin stiffness coefficient to be 85 meV Å^2. Several experiments have reported the spin stiffness of CrO_2, including 150 meV Å^2 [62], 90 meV Å^2 [63], 112.5 meV Å^2 [64], and 91 meV Å^2 [65]. All these values agree well with our calculated result.

For comparison and a demonstration, we introduce additional (static) electron correlation within the LSDA + U formalism [66,67] in both the ground-state calculation and subsequent DFPT calculations, with $U^{\mathrm{eff}} = 2.1$ eV [68]. As shown in the inset of Fig. 3(c), the gapless Goldstone mode is intact in the LSDA + U calculations. This is expected, given that the total energy functional of LSDA + U formalism,

$$E^{\mathrm{tot}} = E^{\mathrm{LSDA}} + \frac{U^{\mathrm{eff}}}{2}\left(\sum_{ma}\varrho^{a0}_{mm} - \frac{1}{2}\sum_{mm'a}\varrho^{a\alpha}_{mm'}\varrho^{a\alpha}_{m'm}\right), \quad (40)$$

is invariant under an arbitrary spin rotation when spin-orbit coupling is not included. The density matrix of d orbitals $\varrho^{a\alpha}_{m'm}$ in the PAW framework is given in Eq. (A14). Spontaneously breaking this continuous symmetry in a ferromagnetic state then leads to gapless Goldstone excitations. The average spin stiffness coefficient is evaluated to be $D = 391$ meV Å^2, almost five times that without the Hubbard U. The energy of the magnon in CrO_2 seems to be highly overestimated in LSDA + U calculations, which can be attributed to the enhanced exchange splitting of the d-orbital dominated bands [5,6].

As a further test, we examine the Goldstone gap as a result of breaking the spin-rotation symmetry by introducing spin-orbit interaction. The atomic spin-orbit interaction for Cr is fairly weak (of the order of tens of meV). Since the gap in the Goldstone magnon is second order in the spin-orbit coupling, it is small for CrO_2. In order to visualize the effect of spin-orbit coupling, we introduce a parameter λ to artificially tune its strength (or speed of light), as in $H = H^0 + \lambda H^{\mathrm{SOC}}$, where

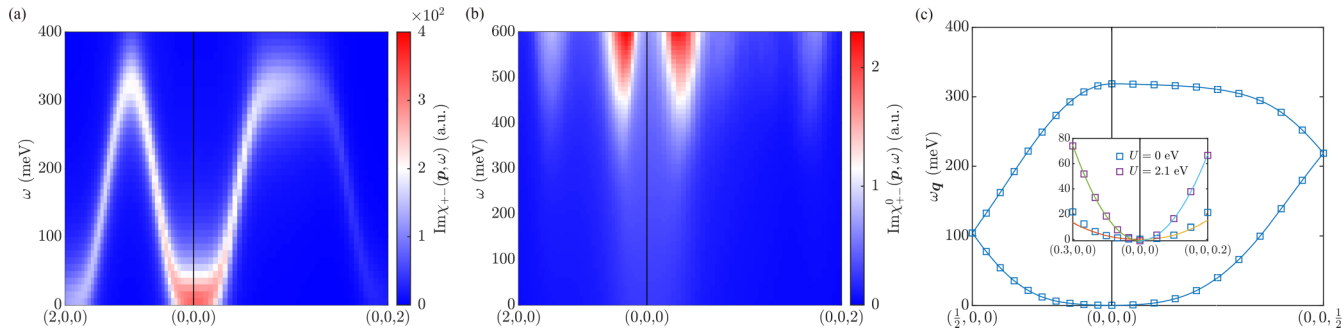

FIG. 3. (a) $\mathrm{Im}\chi_{+-}(\boldsymbol{p},\omega)$ and (b) $\mathrm{Im}\chi^0_{+-}(\boldsymbol{p},\omega)$ of CrO_2 along the [100] and [001] directions. The black vertical line indicates the center of the first Brillouin zone. (c) The folded magnon energy dispersion $\omega_{\boldsymbol{q}}$ of CrO_2 in the first Brillouin zone, extracted from Im χ_{+-} shown in (a). The inset shows the quadratic fits to $\omega_{\boldsymbol{q}}$ at small q along the [100] and [001] directions, respectively, for calculations without Hubbard U correction and with $U^{\mathrm{eff}} = 2.1$ eV. The squares are the calculated data.

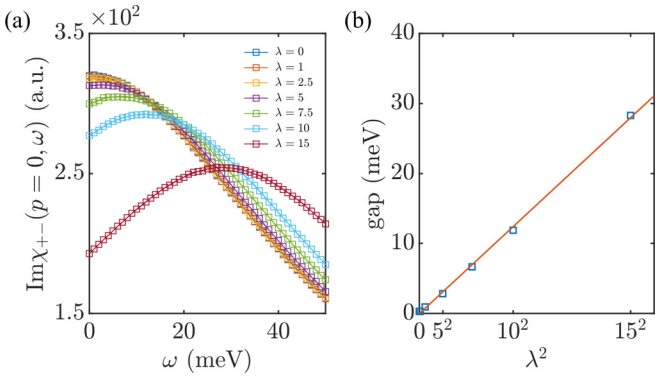

FIG. 4. (a) $\mathrm{Im}\chi_{+-}(p=0,\omega)$ as a function of ω for different λ values. $\lambda = 1$ corresponds to the actual strength of spin-orbit coupling in CrO_2. The squares are the calculated data and the solid lines are the fits with Lorentzian line shape. (b) The Goldstone gap as a function of λ^2 in CrO_2. The solid line is the linear fit.

$\lambda = 1$ corresponds to the actual strength of spin-orbit coupling in CrO_2. The calculated $\mathrm{Im}\chi_{+-}(p=0,\omega)$ as a function of ω for different λ values are shown in Fig. 4(a). Apparently there is a blueshift of the Goldstone mode with increasing λ, indicating the emergence of a Goldstone gap. The Goldstone gap indeed shows a quadratic dependence on λ, as demonstrated by the gap-vs-λ^2 plot in Fig. 4(b). The extrapolated Goldstone gap in CrO_2 is about 0.1 meV.

B. Heusler intermetallic Cu_2MnAl

The ternary intermetallic Cu_2MnAl is a Mn-based full-Heusler alloy with the $L2_1$ structure type (see inset in Fig. 5). The experimental lattice parameter for the conventional cubic cell (space group $Fm\bar{3}m$) is $a = 5.968$ Å [69]. Cu_2MnAl is ferromagnetic below the relatively high Curie temperature (603 K) [69]. Apart from being regarded as a prototype for understanding the electronic correlations in Heusler intermetallics [70], Cu_2MnAl is also being used as a neutron polarizer and monochromator material [71,72].

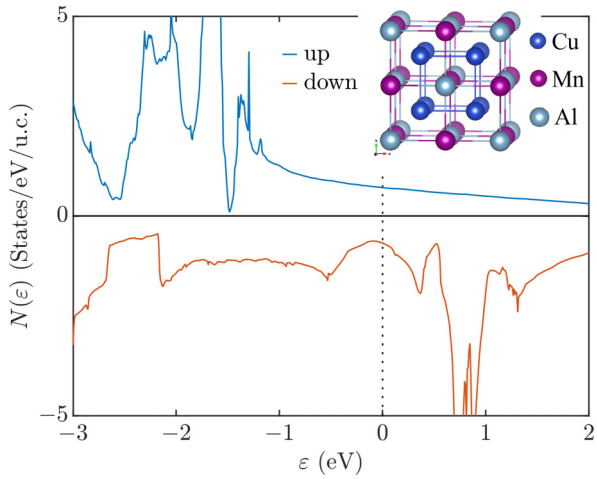

FIG. 5. Spin-resolved densities of states of Cu_2MnAl. Inset: The crystal structure of full Heusler Cu_2MnAl, showing a conventional cubic unit cell for the $L2_1$ structure.

A plane-wave energy cutoff of 350 eV and a $15 \times 15 \times 15$ Γ-centered $\boldsymbol{k}$-grid are used in our calculations. Spin-orbit coupling is not included. The spin-resolved densities of states of Cu_2MnAl computed from the collinear spin-polarized calculation confirms the ferromagnetism of Cu_2MnAl, as shown in Fig. 5. The magnetic moment is primarily carried by Mn atoms and computed to be 3.4 μ_B/Mn. The transverse spin susceptibility $\chi_{+-}(\boldsymbol{p},\omega)$ along the [100], [110], and [111] crystallographic directions is then computed in noncollinear calculations for $\omega \leqslant 300$ meV in 5 meV intervals, with a broadening parameter η of 50 meV.

Figure 6(a) shows the computed magnon spectral function $\mathrm{Im}\chi_{+-}(\boldsymbol{p},\omega)$ along the three principal directions. The acoustic magnon branch is seen clearly only at low energies near the Brillouin zone center. The spectral peaks of these low-energy modes can be adequately fitted with the Lorentzian line shape as in the CrO_2 case. The dispersion of the long-wavelength modes is quadratic and isotropic, as demonstrated in the inset of Fig. 6(c). A spin stiffness coefficient $D = 268$ meV Å^2 is procured from the quadratic fit, which is about 1.5 times larger than the experimental value of 175 meV Å^2 [74].

Notably, at higher energies and near Brillouin zone boundaries, the magnon peaks become fuzzier and broader, attesting to substantial Landau damping in this material. The strong Landau damping is consistent with the presence of the Stoner continuum shown in Fig. 6(b). In stark contrast to the CrO_2 case with almost no Landau damping, the coupling to the Stoner continuum in Cu_2MnAl bestows a magnon peak at a given $\boldsymbol{p}$, an asymmetric profile that defies a Lorentzian fit (see Appendix C). Viewing the coupling to the Stoner continuum as a Fano-type resonance, we superimpose a linear function on the Lorentzian to describe the asymmetric line shape,

$$A(\boldsymbol{p},\omega) = \frac{a_{\boldsymbol{p}}\eta_{\boldsymbol{p}}}{(\omega-\omega_{\boldsymbol{p}})^2+\eta_{\boldsymbol{p}}^2} + \xi_{\boldsymbol{p}}(\omega-\omega_{\boldsymbol{p}}), \tag{41}$$

with $\omega_{\boldsymbol{p}}$, $a_{\boldsymbol{p}}$, $\eta_{\boldsymbol{p}}$, and $\xi_{\boldsymbol{p}}$ as fitting parameters.

As it turns out, this simple modification leads to satisfactory fitting for the entire spectrum, as evidenced in Appendix C. The extracted magnon dispersion is then shown in Fig. 6(c), which coincides with the calculated results of Buczek *et al.* [18,73] and agrees well with the experimental observations along the [100] direction [74]. Along the [110] and [111] directions where the Landau damping seems more pronounced, our computed dispersion shows significant discrepancy from the experimental one. For low-energy modes, $\eta_{\boldsymbol{p}}$ is dominated by the artificial broadening parameter η and the asymmetry is small, as shown in Fig. 6(d). With increasing energies, however, the broadening quickly exceeds η and the asymmetry becomes pronounced, especially near Brillouin zone boundaries, both providing quantitative characterization of the Landau damping.

IV. SUMMARY AND OUTLOOK

In conclusion, we report an implementation of the DFPT method in the PAW framework, which is capable of computing the full linear susceptibilities of real materials. A nested iterative procedure is employed to self-consistently solve the Sternheimer equations, to procure linear susceptibilities along with the first-order wave functions and densities in monochro-

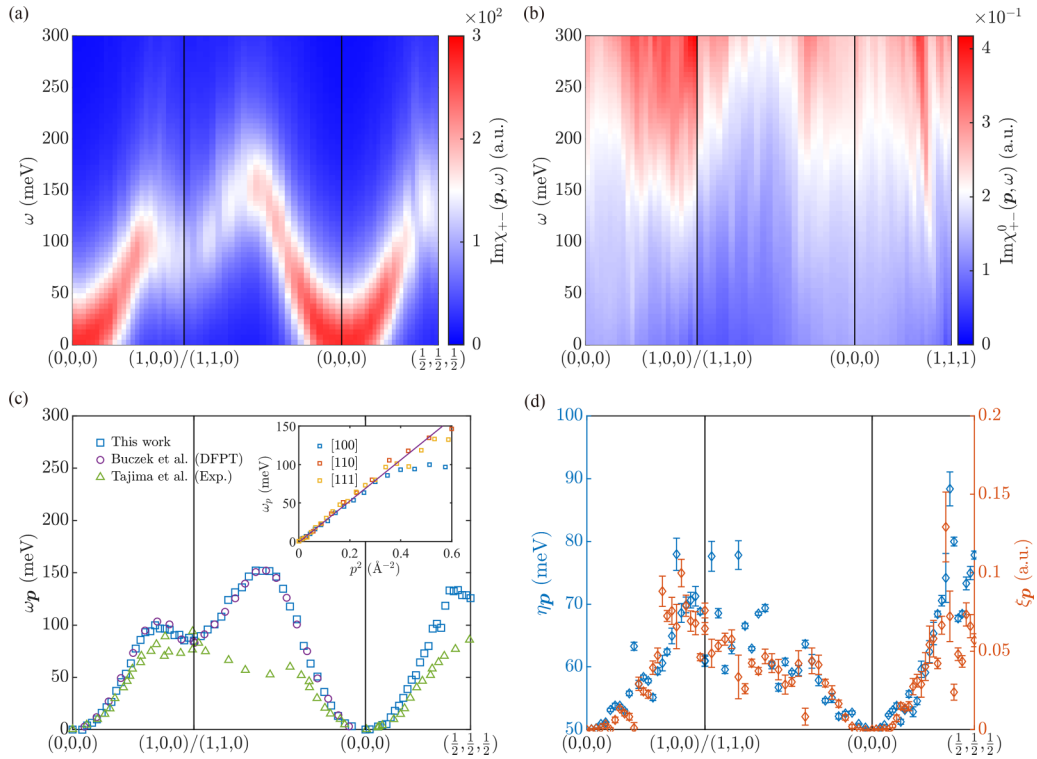

FIG. 6. (a) $\mathrm{Im}\chi_{+-}(\boldsymbol{p},\omega)$ and (b) $\mathrm{Im}\chi^0_{+-}(\boldsymbol{p},\omega)$ of Cu_2MnAl along the [100], [110], and [111] directions. Reciprocal lattice vectors of a conventional cubic cell are adopted here. (c) The magnon energy dispersion $\omega_{\boldsymbol{p}}$ of Cu_2MnAl along the [100], [110], and [111] directions, extracted from the asymmetric Lorentzian fits. ◯ is the calculated data of Buczek *et al.* [18,73], using the Dyson scheme. △ is the experimental data of Tajima *et al.* [74]. Inset: The quadratic fit to the long-wavelength acoustic magnons. (d) Broadening $\eta_{\boldsymbol{p}}$ and asymmetry $\xi_{\boldsymbol{p}}$ of the magnon peaks in Cu_2MnAl along the [100], [110], and [111] directions. The error bars show 95% confidence bounds on the fitting parameters from the fits.

matic and periodic external electromagnetic fields. The time cost of each DFPT calculation (given an external field direction, momentum, and frequency) is comparable to that of a corresponding Kohn-Sham DFT calculation.

As a demonstration, we compute the spin-wave spectra for CrO_2 and Cu_2MnAl. Gapless magnon dispersion is obtained for both materials from the calculations without spin-orbit coupling. The spin stiffness coefficients extracted from the quadratic fits are in agreement with experimental values for both CrO_2 and Cu_2MnAl. The Landau damping in CrO_2 is insignificant due to its half-metallic nature, while in Cu_2MnAl, it is remarkable at high energies and can be quantified with a simple asymmetric Lorentzian fit. The LSDA+U method as well as the effect of spin-orbit coupling are examined in CrO_2, from which the former highly overestimates the magnon energy, while the latter gives rise to a Goldstone gap that is quadratic in spin-orbit coupling strength λ. In order to further validate our implementation, we also compare our result on bcc Fe with previous theoretical and experimental studies, which shows a good agreement, in Appendix D.

There is clearly room for future developments to make the current implementation more efficient and versatile. From an algorithm viewpoint, the occupied subspace is not projected out in Sternheimer equations in the current implementation. As the contribution to the first-order wave functions from the occupied states does not contribute to the first-order densities, projecting out the occupied subspace [15] can potentially improve the efficiency and stability of the nested iteration. As an additional benefit of the projection, it also renders the principle integrals explicit and amenable to analytic techniques, which can further reduce the number of $\boldsymbol{k}$ points required and improve efficiencies. Alternative iterative techniques should be tested in general, for both inner and outer loops, especially in conjunction with the projection.

From a physics viewpoint, a few tasks are on the immediate agenda and new possibilities are clearly on the horizon, beyond the initial demonstrations presented herein. For the spin-wave spectral functions, it will be valuable to compare the computed spectra with experimental results for more materials. A particularly interesting comparison can be made between the dispersion relations obtained *ab initio* from our DFPT implementation and those from Heisenberg models parametrized from constrained DFT energies on the basis of the magnetic force theorem [75–77]. Such comparisons should be examined in detail for materials in the localized and the itinerant limits, as well as for the continuum falling in between. Further systematic studies for the gradient correction (as in generalized gradient approximations) and for the Hubbard correction in the LSDA + U method can reveal the effect of correlation on the spin-wave spectra. As the first-order wave functions are also produced in our code, it is also tempting to evaluate other physical properties, related to density and current responses, such as the magnetoelectric coupling and related transport coefficients. A particular connection may be

made by observing that

$$W = f + f\chi f \tag{42}$$

is the screened kernel, which now includes the charge, spin, and cross screening effects. This will enable one to analyze the many-electron effects in magnetic materials with strong spin-orbit coupling, and potentially evaluate novel bound states from the screened charge/spin interactions.

ACKNOWLEDGMENTS

We acknowledge the financial support from the National Natural Science Foundation of China (Grants No. 11725415 and No. 12274003), the National Key R&D Program of China (Grants No. 2018YFA0305601 and No. 2021YFA1400100), and the Innovation Program for Quantum Science and Technology (Grant No. 2021ZD0302600).

APPENDIX A: HAMILTONIAN IN PAW METHOD

Here we briefly introduce the implementation of PAW method in VASP, including the spin-orbit coupling and LSDA + U method, to complement the discussions in the paper. For further details, please refer to Refs. [31,32].

The overlap operator is defined by

$$S = 1 + \sum_{ija} |\tilde{p}_i^a\rangle q_{ij}^a \langle \tilde{p}_j^a|, \tag{A1}$$

with

$$q_{ij}^a = \langle \phi_i^a | \phi_j^a \rangle - \langle \tilde{\phi}_i^a | \tilde{\phi}_j^a \rangle. \tag{A2}$$

The Hamiltonian of the Kohn-Sham equation is given by

$$\tilde{H} = -\frac{1}{2}\Delta + \tilde{v}^{\text{eff}} + \sum_{ija} |\tilde{p}_i^a\rangle (\hat{D}_{ij}^a + \tilde{D}_{ij}^a) \langle \tilde{p}_j^a|, \tag{A3}$$

with $\tilde{D}_{ij}^a = D_{ij}^{a,1} - \tilde{D}_{ij}^{a,1}$.

The local potential $\tilde{v}^{\text{eff}}$ involves the Hartree and xc terms,

$$\tilde{v}^{\text{eff}} = v^{\text{H}}[\tilde{n} + \hat{n} + \tilde{n}_{\text{Zc}}] + v^{\text{xc}}[\tilde{n} + \hat{n} + \tilde{n}_{\text{c}}]. \tag{A4}$$

The partial electronic core density $\tilde{n}_{\text{c}}$ and pseudized core density $\tilde{n}_{\text{Zc}}$ are frozen. The pseudodensity $\tilde{n}$ and compensation density $\hat{n}$ have been shown in Eq. (27), with $\hat{n}(\boldsymbol{r})$ defined via $\hat{Q}_{ij}^a(\boldsymbol{r})$:

$$\begin{aligned} Q_{ij}^{a\alpha}(\boldsymbol{r}) &= \phi_i^{a\dagger}(\boldsymbol{r})\sigma_\alpha \phi_j^a(\boldsymbol{r}) - \tilde{\phi}_i^{a\dagger}(\boldsymbol{r})\sigma_\alpha \tilde{\phi}_j^a(\boldsymbol{r}), \\ q_{ij}^{aL\alpha} &= \int Q_{ij}^{a\alpha}(\boldsymbol{r}) |\boldsymbol{r} - \boldsymbol{R}_a|^l Y_L^*(\widehat{\boldsymbol{r} - \boldsymbol{R}_a}) d\boldsymbol{r}, \\ \hat{Q}_{ij}^{a\alpha}(\boldsymbol{r}) &= \sum_L q_{ij}^{aL\alpha} g_l(|\boldsymbol{r} - \boldsymbol{R}_a|) Y_L(\widehat{\boldsymbol{r} - \boldsymbol{R}_a}). \end{aligned} \tag{A5}$$

Here, $Q_{ij}^a(\boldsymbol{r})$, q_{ij}^{aL}, and $\hat{Q}_{ij}^a(\boldsymbol{r})$ are all four-vectors, and L is a shorthand for (l, m).

$\hat{D}_{ij}^a$ is given by

$$\hat{D}_{ij}^a = \int_{\Omega_a} \tilde{v}_\alpha^{\text{eff}}(\boldsymbol{r}) \hat{Q}_{ij}^{a\alpha}(\boldsymbol{r}) d\boldsymbol{r}, \tag{A6}$$

with $\tilde{v}_\alpha^{\text{eff}}(\boldsymbol{r}) = \frac{1}{2}\,\text{tr}\{\sigma_\alpha \tilde{v}^{\text{eff}}(\boldsymbol{r})\}$. The terms $D_{ij}^{a,1}$ and $\tilde{D}_{ij}^{a,1}$ are given by

$$\begin{aligned} D_{ij}^{a,1} &= \langle \phi_i^a | -\frac{1}{2}\Delta + v_1^{\text{eff}} | \phi_j^a \rangle, \\ \tilde{D}_{ij}^{a,1} &= \langle \tilde{\phi}_i^a | -\frac{1}{2}\Delta + \tilde{v}_1^{\text{eff}} | \tilde{\phi}_j^a \rangle + \int \tilde{v}_{\alpha,1}^{\text{eff}}(\boldsymbol{r}) Q_{ij}^{a\alpha}(\boldsymbol{r}) d\boldsymbol{r}, \end{aligned} \tag{A7}$$

with

$$\begin{aligned} v_1^{\text{eff}}[n^1] &= v^{\text{H}}[n^1 + n_{\text{Zc}}] + v^{\text{xc}}[n^1 + n_{\text{c}}], \\ \tilde{v}_1^{\text{eff}}[\tilde{n}^1] &= v^{\text{H}}[\tilde{n}^1 + \hat{n} + \tilde{n}_{\text{Zc}}] + v^{\text{xc}}[\tilde{n}^1 + \hat{n} + \tilde{n}_{\text{c}}]. \end{aligned} \tag{A8}$$

The on-site densities n^1 and $\tilde{n}^1$ are

$$\begin{aligned} n_\alpha^1(\boldsymbol{r}) &= \sum_{ija} \varrho_{ij}^a \phi_i^{a\dagger}(\boldsymbol{r}) \sigma_\alpha \phi_j^a(\boldsymbol{r}), \\ \tilde{n}_\alpha^1(\boldsymbol{r}) &= \sum_{ija} \varrho_{ij}^a \tilde{\phi}_i^{a\dagger}(\boldsymbol{r}) \sigma_\alpha \tilde{\phi}_j^a(\boldsymbol{r}). \end{aligned} \tag{A9}$$

It is then clear that $\tilde{D}_{ij}^a = D_{ij}^{a,1} - \tilde{D}_{ij}^{a,1}$ is a function of density matrix ϱ^a.

The spin-orbit coupling in the PAW method is given by [78]

$$\tilde{H}^{\text{SOC}} = \sum_{ija} |\tilde{p}_i^a\rangle D_{ij}^{a,\text{SOC}} \langle \tilde{p}_j^a|, \tag{A10}$$

with

$$\begin{aligned} D_{ij}^{a,\text{SOC}} &= \langle \phi_i^a | \frac{\alpha^2}{4} \frac{K(r)}{r} \frac{dv_1^{\text{eff}}(r)}{dr} \boldsymbol{\sigma} \cdot \boldsymbol{L} | \phi_j^a \rangle, \\ K(r) &= \left(1 - \frac{\alpha^2 v_1^{\text{eff}}(r)}{2}\right)^{-2}. \end{aligned} \tag{A11}$$

Here, $v_1^{\text{eff}}(r)$ is the spherical part of the effective AE potential and α is the fine-structure constant. As seen from Eqs. (A8) and (A9), $v_1^{\text{eff}}(r)$ is determined by ϱ^a.

The Hubbard correction of LSDA + U formalism in the PAW method is given by [66,67]

$$\tilde{H}^U = \sum_{ija} |\tilde{p}_i^a\rangle D_{ij}^{a,U} \langle \tilde{p}_j^a|, \tag{A12}$$

and the nonlocal potential $D_{ij}^{a,U}$ is

$$D_{ij}^{a,U} = \sum_\alpha \frac{U_{\text{eff}}}{2} (\delta_{\alpha 0}\delta_{mm'} - \varrho_{m'm}^{a\alpha}) \langle \phi_{nls}^a | \sigma^\alpha | \phi_{n'l's'}^a \rangle, \tag{A13}$$

with

$$\varrho_{m'm}^{a\alpha} = \sum_{ns,n's'} \varrho_{ij}^a \langle \phi_{nls}^a | \sigma^\alpha | \phi_{n'l's'}^a \rangle. \tag{A14}$$

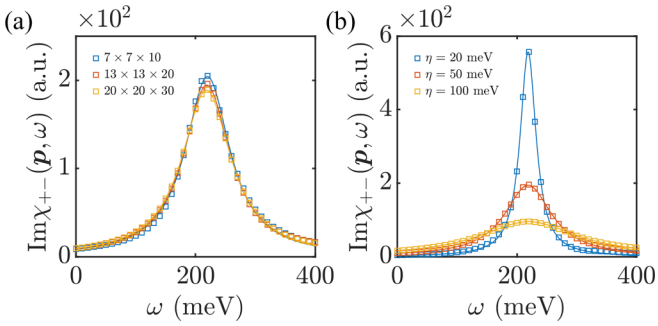

FIG. 7. $\mathrm{Im}\chi_{+-}(\boldsymbol{p},\omega)$ as a function of ω for different (a) $\boldsymbol{k}$-point meshes and (b) η in CrO_2 with $\boldsymbol{p} = (0, 0, 0.5)$. The squares are the calculated data and the solid lines are the fits with Lorentzian line shape. In (a), η is set to be 50 meV. In (b), a $13 \times 13 \times 20$ Γ-centered mesh of $\boldsymbol{k}$ points is used.

Here, $i = (nlms)$ and $j = (n'l'm's')$, with l and l' restricted to 2 for d orbitals. $|\phi^a_{nls}\rangle$ is the radial part of $|\phi^a_i\rangle$. Again, both $D^{a,\mathrm{SOC}}_{ij}$ and $D^{a,U}_{ij}$ are functions of density matrix ϱ^a.

APPENDIX B: CONVERGENCE

We examine the convergence of $\mathrm{Im}\chi_{+-}$ with respect to the $\boldsymbol{k}$-point mesh and the effect of broadening parameter η introduced in Eq. (15), as shown in Fig. 7. In Fig. 7(a), the values of $\mathrm{Im}\chi_{+-}(\boldsymbol{p},\omega)$ decrease slightly when increasing the number of $\boldsymbol{k}$ points, while the location of the peak remains unchanged. The extracted magnon energies for different $\boldsymbol{k}$-point meshes are 219.8 meV ($7 \times 7 \times 10$), 218.7 meV ($13 \times 13 \times 20$), and 218.2 meV ($20 \times 20 \times 30$). In Fig. 7(b), the peak value of $\mathrm{Im}\chi_{+-}(\boldsymbol{p},\omega)$ is inversely proportional to η with its location independent of η. A small η slows convergence.

APPENDIX C: ASYMMETRIC LORENTZIAN FITTING

We examine the symmetric and asymmetric Lorentzian fittings for Cu_2MnAl in Fig. 8.

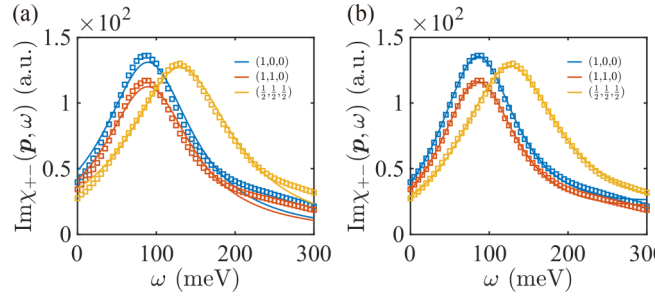

FIG. 8. (a),(b) $\mathrm{Im}\chi_{+-}(\boldsymbol{p},\omega)$ as a function of ω for $\boldsymbol{p} = (1, 0, 0)$, (1,1,0), and (1,1,1) in Cu_2MnAl. The squares are the calculated data. The solid lines are the fits with (a) symmetric or (b) asymmetric Lorentzian function.

APPENDIX D: BENCHMARK ON BCC FE

We perform a benchmark with body-centered cubic (bcc) Fe, of which the computed spin-wave spectrum is shown in Fig. 9.

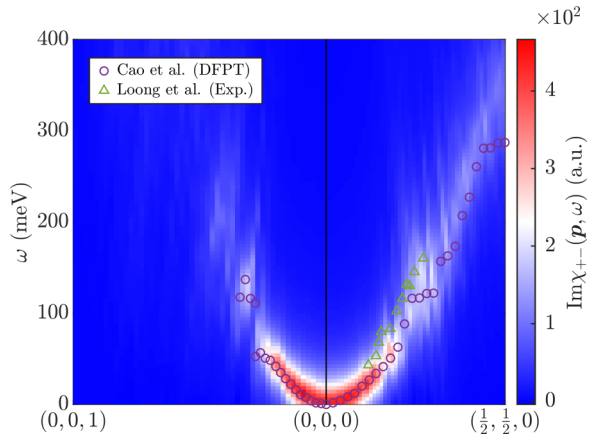

FIG. 9. $\mathrm{Im}\chi_{+-}(\boldsymbol{p},\omega)$ of bcc Fe along the [001] and [110] directions. Reciprocal lattice vectors of a conventional cubic cell are adopted here. ◯ is the calculated data of Cao *et al.* [20] and △ is the experimental data of Loong *et al.* [79].

[1] R. Kubo, Statistical-mechanical theory of irreversible processes. I. General theory and simple applications to magnetic and conduction problems, J. Phys. Soc. Jpn. **12**, 570 (1957).

[2] W. Kohn and L. J. Sham, Self-consistent equations including exchange and correlation effects, Phys. Rev. **140**, A1133 (1965).

[3] E. Runge and E. K. U. Gross, Density-Functional Theory for Time-Dependent Systems, Phys. Rev. Lett. **52**, 997 (1984).

[4] E. K. U. Gross and W. Kohn, Local Density-Functional Theory of Frequency-Dependent Linear Response, Phys. Rev. Lett. **55**, 2850 (1985).

[5] K. Karlsson and F. Aryasetiawan, Spin-wave excitation spectra of nickel and iron, Phys. Rev. B **62**, 3006 (2000).

[6] E. Şaşıoğlu, A. Schindlmayr, C. Friedrich, F. Freimuth, and S. Blügel, Wannier-function approach to spin excitations in solids, Phys. Rev. B **81**, 054434 (2010).

[7] H. Okumura, K. Sato, and T. Kotani, Spin-wave dispersion of 3*d* ferromagnets based on quasiparticle self-consistent *GW* calculations, Phys. Rev. B **100**, 054419 (2019).

[8] H. Okumura, K. Sato, K. Suzuki, and T. Kotani, Electronic structure and spin-wave dispersion of Cu_2MnAl, Ni_2MnSn, and Pd_2MnSn based on quasiparticle self-consistent *GW* calculations, J. Phys. Soc. Jpn. **89**, 034704 (2020).

[9] M. S. Hybertsen and S. G. Louie, *Ab initio* static dielectric matrices from the density-functional approach. I. Formulation and application to semiconductors and insulators, Phys. Rev. B **35**, 5585 (1987).

[10] M. Gajdoš, K. Hummer, G. Kresse, J. Furthmüller, and F. Bechstedt, Linear optical properties in the projector-augmented wave methodology, Phys. Rev. B **73**, 045112 (2006).

[11] H.-C. Weissker, J. Serrano, S. Huotari, E. Luppi, M. Cazzaniga, F. Bruneval, F. Sottile, G. Monaco, V. Olevano, and L. Reining, Dynamic structure factor and dielectric function of silicon for

finite momentum transfer: Inelastic x-ray scattering experiments and *ab initio* calculations, Phys. Rev. B **81**, 085104 (2010).
[12] M. Cazzaniga, H.-C. Weissker, S. Huotari, T. Pylkkänen, P. Salvestrini, G. Monaco, G. Onida, and L. Reining, Dynamical response function in sodium and aluminum from time-dependent density-functional theory, Phys. Rev. B **84**, 075109 (2011).
[13] I. Timrov, N. Vast, R. Gebauer, and S. Baroni, Electron energy loss and inelastic x-ray scattering cross sections from time-dependent density-functional perturbation theory, Phys. Rev. B **88**, 064301 (2013).
[14] P. Giannozzi, S. de Gironcoli, P. Pavone, and S. Baroni, *Ab initio* calculation of phonon dispersions in semiconductors, Phys. Rev. B **43**, 7231 (1991).
[15] S. Baroni, S. de Gironcoli, A. Dal Corso, and P. Giannozzi, Phonons and related crystal properties from density-functional perturbation theory, Rev. Mod. Phys. **73**, 515 (2001).
[16] A. Dal Corso, Density functional perturbation theory within the projector augmented wave method, Phys. Rev. B **81**, 075123 (2010).
[17] S. Y. Savrasov, Linear Response Calculations of Spin Fluctuations, Phys. Rev. Lett. **81**, 2570 (1998).
[18] P. Buczek, A. Ernst, P. Bruno, and L. M. Sandratskii, Energies and Lifetimes of Magnons in Complex Ferromagnets: A First-Principle Study of Heusler Alloys, Phys. Rev. Lett. **102**, 247206 (2009).
[19] B. Rousseau, A. Eiguren, and A. Bergara, Efficient computation of magnon dispersions within time-dependent density functional theory using maximally localized Wannier functions, Phys. Rev. B **85**, 054305 (2012).
[20] K. Cao, H. Lambert, P. G. Radaelli, and F. Giustino, *Ab initio* calculation of spin fluctuation spectra using time-dependent density functional perturbation theory, plane waves, and pseudopotentials, Phys. Rev. B **97**, 024420 (2018).
[21] T. Gorni, I. Timrov, and S. Baroni, Spin dynamics from time-dependent density functional perturbation theory, Eur. Phys. J. B **91**, 249 (2018).
[22] N. Tancogne-Dejean, F. G. Eich, and A. Rubio, Time-dependent magnons from first principles, J. Chem. Theor. Comput. **16**, 1007 (2020).
[23] N. Singh, P. Elliott, J. K. Dewhurst, E. K. U. Gross, and S. Sharma, *Ab initio* real-time magnon dynamics in ferromagnetic and ferrimagnetic systems, Phys. Status Solidi B **257**, 1900654 (2020).
[24] T. Skovhus and T. Olsen, Dynamic transverse magnetic susceptibility in the projector augmented-wave method: Application to Fe, Ni, and Co, Phys. Rev. B **103**, 245110 (2021).
[25] M. S. Hybertsen and S. G. Louie, Electron correlation in semiconductors and insulators: Band gaps and quasiparticle energies, Phys. Rev. B **34**, 5390 (1986).
[26] M. Shishkin and G. Kresse, Implementation and performance of the frequency-dependent *GW* method within the PAW framework, Phys. Rev. B **74**, 035101 (2006).
[27] M. Shishkin and G. Kresse, Self-consistent *GW* calculations for semiconductors and insulators, Phys. Rev. B **75**, 235102 (2007).
[28] T. Skovhus, T. Olsen, and H. M. Rønnow, Influence of static correlation on the magnon dynamics of an itinerant ferromagnet with competing exchange interactions: First-principles study of MnBi, Phys. Rev. Mater. **6**, 054402 (2022).
[29] D. R. Hamann, M. Schlüter, and C. Chiang, Norm-Conserving Pseudopotentials, Phys. Rev. Lett. **43**, 1494 (1979).
[30] D. Vanderbilt, Soft self-consistent pseudopotentials in a generalized eigenvalue formalism, Phys. Rev. B **41**, 7892 (1990).
[31] P. E. Blöchl, Projector augmented-wave method, Phys. Rev. B **50**, 17953 (1994).
[32] G. Kresse and D. Joubert, From ultrasoft pseudopotentials to the projector augmented-wave method, Phys. Rev. B **59**, 1758 (1999).
[33] G. Kresse and J. Furthmüller, Efficient iterative schemes for *ab initio* total-energy calculations using a plane-wave basis set, Phys. Rev. B **54**, 11169 (1996).
[34] P. Giannozzi Jr, O. Andreussi, T. Brumme, O. Bunau, M. B. Nardelli, M. Calandra, R. Car, C. Cavazzoni, D. Ceresoli, M. Cococcioni *et al.*, Advanced capabilities for materials modelling with QUANTUM ESPRESSO, J. Phys.: Condens. Matter **29**, 465901 (2017).
[35] X. Gonze, B. Amadon, G. Antonius, F. Arnardi, L. Baguet, J.-M. Beuken, J. Bieder, F. Bottin, J. Bouchet, E. Bousquet *et al.*, The Abinit project: Impact, environment and recent developments, Comput. Phys. Commun. **248**, 107042 (2020).
[36] $e = \hbar = m_e = 1$.
[37] G. Vignale and W. Kohn, Current-Dependent Exchange-Correlation Potential for Dynamical Linear Response Theory, Phys. Rev. Lett. **77**, 2037 (1996).
[38] G. Vignale, C. A. Ullrich, and S. Conti, Time-Dependent Density Functional Theory Beyond the Adiabatic Local Density Approximation, Phys. Rev. Lett. **79**, 4878 (1997).
[39] F. Kootstra, P. L. de Boeij, and J. G. Snijders, Application of time-dependent density-functional theory to the dielectric function of various nonmetallic crystals, Phys. Rev. B **62**, 7071 (2000).
[40] M. van Faassen, P. L. de Boeij, R. van Leeuwen, J. A. Berger, and J. G. Snijders, Ultranonlocality in Time-Dependent Current-Density-Functional Theory: Application to Conjugated Polymers, Phys. Rev. Lett. **88**, 186401 (2002).
[41] M. A. Marques, C. A. Ullrich, F. Nogueira, A. Rubio, K. Burke, and E. K. U. Gross, *Time-dependent Density Functional Theory* (Springer Berlin, Heidelberg, 2006).
[42] T. Ando, Inter-subband optical absorption in space-charge layers on semiconductor surfaces, Z. Phys. B **26**, 263 (1977).
[43] A. Zangwill and P. Soven, Density-functional approach to local-field effects in finite systems: Photoabsorption in the rare gases, Phys. Rev. A **21**, 1561 (1980).
[44] A. Zangwill and P. Soven, Resonant Photoemission in Barium and Cerium, Phys. Rev. Lett. **45**, 204 (1980).
[45] Here, $\boldsymbol{B}$ is the Zeeman field. We ignore the nonlocal coupling between the magnetic field and orbitals, which requires the current density functional theory and is beyond the scope of the present work.
[46] R. M. Sternheimer, Electronic polarizabilities of ions from the Hartree-Fock wave functions, Phys. Rev. **96**, 951 (1954).
[47] S. de Gironcoli, Lattice dynamics of metals from density-functional perturbation theory, Phys. Rev. B **51**, 6773 (1995).
[48] F. Giustino, M. L. Cohen, and S. G. Louie, *GW* method with the self-consistent SternHeimer equation, Phys. Rev. B **81**, 115105 (2010).
[49] C. G. Broyden, A class of methods for solving nonlinear simultaneous equations, Math. Comp. **19**, 577 (1965).

[50] D. D. Johnson, Modified Broyden's method for accelerating convergence in self-consistent calculations, Phys. Rev. B **38**, 12807 (1988).

[51] As will be explained later, in our implementation, the exact solution is used to quickly correct the contributions of the occupied and a small number of low-lying particle states in the iterative solution of the Sternheimer equations.

[52] P. Pulay, Convergence acceleration of iterative sequences. The case of scf iteration, Chem. Phys. Lett. **73**, 393 (1980).

[53] D. M. Wood and A. Zunger, A new method for diagonalising large matrices, J. Phys. A: Math. Gen. **18**, 1343 (1985).

[54] H. A. Mook and R. M. Nicklow, Neutron scattering investigation of the magnetic excitations in iron, Phys. Rev. B **7**, 336 (1973).

[55] L. Braicovich, L. J. P. Ament, V. Bisogni, F. Forte, C. Aruta, G. Balestrino, N. B. Brookes, G. M. De Luca, P. G. Medaglia, F. Miletto Granozio, M. Radovic, M. Salluzzo, J. van den Brink, and G. Ghiringhelli, Dispersion of Magnetic Excitations in the Cuprate La_2CuO_4 and $CaCuO_2$ Compounds Measured Using Resonant X-ray Scattering, Phys. Rev. Lett. **102**, 167401 (2009).

[56] L. J. P. Ament, M. van Veenendaal, T. P. Devereaux, J. P. Hill, and J. van den Brink, Resonant inelastic x-ray scattering studies of elementary excitations, Rev. Mod. Phys. **83**, 705 (2011).

[57] K. Schwarz, CrO_2 predicted as a half-metallic ferromagnet, J. Phys. F **16**, L211 (1986).

[58] W. H. Cloud, D. Schreiber, and K. Babcock, X-ray and magnetic studies of CrO_2 single crystals, J. Appl. Phys. **33**, 1193 (1962).

[59] A. Singh, C. Jansen, K. Lahabi, and J. Aarts, High-Quality CrO_2 Nanowires for Dissipation-Less Spintronics, Phys. Rev. X **6**, 041012 (2016).

[60] M. Rabe, J. Dreßen, D. Dahmen, J. Pommer, H. Stahl, U. Rüdiger, G. Güntherodt, S. Senz, and D. Hesse, Preparation and characterization of thin ferromagnetic CrO_2 films for applications in magnetoelectronics, J. Magn. Magn. Mater. **211**, 314 (2000).

[61] P. E. Blöchl, O. Jepsen, and O. K. Andersen, Improved tetrahedron method for Brillouin-zone integrations, Phys. Rev. B **49**, 16223 (1994).

[62] A. Barry, J. M. D. Coey, L. Ranno, and K. Ounadjela, Evidence for a gap in the excitation spectrum of CrO_2, J. Appl. Phys. **83**, 7166 (1998).

[63] X. W. Li, A. Gupta, and G. Xiao, Influence of strain on the magnetic properties of epitaxial (100) chromium dioxide (CrO_2) films, Appl. Phys. Lett. **75**, 713 (1999).

[64] S. M. Watts, Magnetotransport in half-metallic ferromagnetic oxides, Ph.D. thesis, Florida State University, 2002.

[65] H. Liu, R. K. Zheng, Y. Wang, H. L. Bai, and X. X. Zhang, Transport and magnetotransport properties of cold-pressed CrO_2 powder, Phys. Stat. Solidi A **202**, 144 (2005).

[66] S. L. Dudarev, G. A. Botton, S. Y. Savrasov, C. J. Humphreys, and A. P. Sutton, Electron-energy-loss spectra and the structural stability of nickel oxide: An LSDA + U study, Phys. Rev. B **57**, 1505 (1998).

[67] A. Rohrbach, J. Hafner, and G. Kresse, Electronic correlation effects in transition-metal sulfides, J. Phys.: Condens. Matter **15**, 979 (2003).

[68] M. A. Korotin, V. I. Anisimov, D. I. Khomskii, and G. A. Sawatzky, CrO_2: A Self-Doped Double Exchange Ferromagnet, Phys. Rev. Lett. **80**, 4305 (1998).

[69] K. Buschow, P. van Engen, and R. Jongebreur, Magneto-optical properties of metallic ferromagnetic materials, J. Magn. Magn. Mater. **38**, 1 (1983).

[70] J. A. Weber, A. Bauer, P. Böni, H. Ceeh, S. B. Dugdale, D. Ernsting, W. Kreuzpaintner, M. Leitner, C. Pfleiderer, and C. Hugenschmidt, Spin-Resolved Fermi Surface of the Localized Ferromagnetic Heusler Compound Cu_2MnAl Measured with Spin-Polarized Positron Annihilation, Phys. Rev. Lett. **115**, 206404 (2015).

[71] A. Delapalme, J. Schweizer, G. Couderchon, and R. Perrier de la Bathie, Study of Heusler alloy (Cu_2MnAl) as monochromator for polarized neutrons, Nucl. Instrum. Methods **95**, 589 (1971).

[72] A. Neubauer, F. Jonietz, M. Meven, R. Georgii, G. Brandl, G. Behr, P. Böni, and C. Pfleiderer, Optical floating zone growth of high-quality Cu_2MnAl single crystals, Nucl. Instrum. Methods Phys. Res., Sect. A **688**, 66 (2012).

[73] P. A. Buczek, Spin dynamics of complex itinerant magnets, Ph.D. thesis, Universitäts- und Landesbibliothek Sachsen-Anhalt, 2009.

[74] K. Tajima, Y. Ishikawa, P. J. Webster, M. W. Stringfellow, D. Tocchetti, and K. R. A. Zeabeck, Spin waves in a Heusler alloy Cu_2MnAl, J. Phys. Soc. Jpn. **43**, 483 (1977).

[75] A. I. Liechtenstein, M. I. Katsnelson, and V. A. Gubanov, Exchange interactions and spin-wave stiffness in ferromagnetic metals, J. Phys. F **14**, L125 (1984).

[76] A. Liechtenstein, M. Katsnelson, V. Antropov, and V. Gubanov, Local spin density functional approach to the theory of exchange interactions in ferromagnetic metals and alloys, J. Magn. Magn. Mater. **67**, 65 (1987).

[77] P. Bruno, Exchange Interaction Parameters and Adiabatic Spin-Wave Spectra of Ferromagnets: A "*Renormalized* Magnetic Force Theorem", Phys. Rev. Lett. **90**, 087205 (2003).

[78] S. Steiner, S. Khmelevskyi, M. Marsmann, and G. Kresse, Calculation of the magnetic anisotropy with projected-augmented-wave methodology and the case study of disordered $Fe_{1-x}Co_x$ alloys, Phys. Rev. B **93**, 224425 (2016).

[79] C. Loong, J. M. Carpenter, J. W. Lynn, R. A. Robinson, and H. A. Mook, Neutron scattering study of the magnetic excitations in ferromagnetic iron at high energy transfers, J. Appl. Phys. **55**, 1895 (1984).